

1      **Modulation of the energetic electron distribution caused by toroidal mode ULF  
2      waves in association with periodic enhancement of whistler-mode chorus emissions**  
3

4      A. Ono<sup>1</sup>, Y. Katoh<sup>1</sup>, M. Teramoto<sup>2</sup>, T. Hori<sup>3</sup>, A. Kumamoto<sup>1</sup>, F. Tsuchiya<sup>1</sup>, Y. Kasaba<sup>1</sup>,

5      K. Isono<sup>1</sup>, Y. Miyoshi<sup>3</sup>, S. Kasahara<sup>4</sup>, Y. Kasahara<sup>5</sup>, S. Matsuda<sup>5</sup>, S. Nakamura<sup>3</sup>,

6      A. Matsuoka<sup>6</sup>, S. Yokota<sup>7</sup>, K. Keika<sup>4</sup>, T. Mitani<sup>8</sup>, I. Shinohara<sup>8</sup>

7      <sup>1</sup>Graduate School of Science, Tohoku University, JAPAN

8      <sup>2</sup> Kyushu Institute of Technology, JAPAN

9      <sup>3</sup> Nagoya University, JAPAN

10     <sup>4</sup> University of Tokyo, JAPAN

11     <sup>5</sup> Kanazawa University, JAPAN

12     <sup>6</sup> Kyoto University, JAPAN

13     <sup>7</sup> Osaka University, JAPAN

14     <sup>8</sup> ISAS/JAXA, JAPAN

15     Corresponding author: Yuto Katoh (yuto.katoh@tohoku.ac.jp)

16

17     **Key Points:**

- 18        • ERG/Arase satellite observation of the simultaneous enhancement of whistler-mode  
19        chorus, toroidal mode ULF waves, and energetic electron flux
- 20        • Flux enhancement of 20-50 keV electrons is observed at the timing of the specific phase  
21        angle of the toroidal mode ULF waves
- 22        • A model for the modulation of the drift speed of energetic electrons by toroidal mode  
23        ULF waves is proposed
- 24

25    **Abstract**

26    ERG/Arase satellite observations show a simultaneous enhancement of whistler-mode chorus  
27    emissions and electron flux associated with toroidal mode ultra-low frequency (ULF) waves. The  
28    satellite observed the intensification of both chorus emissions and electron flux in the energy  
29    range satisfying the cyclotron resonance condition during the westward oscillation phase of the  
30    toroidal mode ULF waves. A model for the observed periodic variations is proposed. We  
31    consider the modulation of the drift speed of energetic electrons to be the  $\mathbf{E}_X \times \mathbf{B}_0$  drift due to  
32    the radial component of the wave electric field  $\mathbf{E}_X$  and the ambient magnetic field  $\mathbf{B}_0$ . Assuming  
33    a wave phase variation of the toroidal mode ULF oscillation in the azimuthal direction, we  
34    expect the accumulation of energetic electrons at locations corresponding to a specific phase  
35    angle, consistent with the observed phase relationship.

36

37    **Plain Language Summary**

38    Whistler-mode chorus emissions, interacting with energetic/relativistic electrons in the very wide  
39    energy range from a few keV to MeV, have been intensively studied for more than a half decade  
40    because of their significance in producing radiation belts and auroral electrons. Chorus emissions  
41    have been known by their periodic enhancement in the time scale of a few seconds to minutes,  
42    although physical processes governing the periodicity have not been fully understood. This paper  
43    analyses the ERG/Arase satellite observation of the simultaneous enhancements of both chorus  
44    emissions and electrons flux under the presence of toroidal mode ULF waves. The enhancement  
45    of both chorus emissions and electron flux is identified at a timing corresponding to the  
46    westward phase of the toroidal mode oscillations. We propose a model considering the

47 modulation of the drift speed of energetic electrons, which consistently explains the observed  
48 phase relationship between electrons and ULF waves.

49

## 50      **1 Introduction**

51           Whistler-mode chorus emissions play significant roles in the acceleration and the loss of  
52           energetic electrons in the terrestrial magnetosphere. Previous studies revealed that chorus  
53           emissions are generated through non-linear wave-particle interaction processes with energetic  
54           electrons (e.g., Omura et al., 2008, 2009; Omura, 2021). It was also revealed that chorus  
55           emissions cause the periodic precipitation of energetic electrons into the atmosphere through  
56           wave-particle interactions, contributing to diffuse and pulsating auroras (e.g., Coroniti and  
57           Kennel, 1970; Nishimura et al., 2010; Miyoshi et al., 2010, 2015, 2021; S. Kasahara et al.,  
58           2018a). While the mechanism controlling the periodicity of the chorus wave generation is one of  
59           the important problems unsolved in magnetospheric physics, the roles of ultra-low frequency  
60           (ULF) waves have been discussed for several decades. Previous studies focusing on the  
61           compressional ULF waves suggested that modulations of the linear growth rate of whistler-mode  
62           waves are responsible for the periodic enhancements of chorus emissions (e.g., Coroniti and  
63           Kennel, 1970; Li et al., 2011; Xia et al., 2016). The modulations of chorus emissions caused by  
64           poloidal and toroidal mode ULF waves are also reported (Jaynes et al., 2015; Liu et al., 2019;  
65           Zhang et al., 2019), while the modulation mechanism by only poloidal mode waves has been  
66           explained based on the drift resonance theory (e.g., Southwood and Kivelson, 1981). Although  
67           the roles of poloidal and compressional ULF waves have been revealed, it is still unclear how  
68           energetic electrons are modulated by toroidal mode waves. Based on the drift resonance theory,  
69           Elkington et al. (1999) discussed the modulation mechanism of MeV electrons caused by  
70           toroidal mode ULF waves assuming that the electron drift path is asymmetric between the noon  
71           sector and the midnight sector due to the compression of the magnetopause. However, how  
72           toroidal mode ULF waves can modulate the distribution of energetic electrons has not been fully

73 understood. In the present study, we analyze substorm-related toroidal mode ULF waves, chorus  
74 emissions, and energetic electrons simultaneously observed by the Exploration of energization  
75 and Radiation in Geospace (ERG, also called Arase) satellite (Miyoshi et al., 2018a) and propose  
76 a model explaining how toroidal mode waves modulate energetic electrons.

## 77 **2 Data and Instruments**

78 The ERG satellite was launched on 20 December 2016 into an elliptical orbit with apogee  
79 and perigee altitudes of 32,000 km and 460 km, respectively, with an inclination angle of 31  
80 degrees (Miyoshi et al., 2018a). We analyzed data obtained by the High Frequency Analyzer  
81 (HFA; Kumamoto et al., 2018; Y. Kasahara et al., 2018d), the Onboard Frequency Analyzer  
82 (OFA; Matsuda et al., 2018; Y. Kasahara et al., 2018c), and the Electric Field Detector (EFD;  
83 Kasaba et al., 2017; Y. Kasahara et al., 2018b) of the Plasma Wave Experiment (PWE; Y.  
84 Kasahara et al., 2018a), the Magnetic Field Experiment (MGF; Matsuoka et al., 2018a; Matsuoka  
85 et al., 2018b), the Medium-Energy Particle Experiments – Electron Analyzer (MEP-e; S.  
86 Kasahara et al., 2018b; S. Kasahara et al., 2018c) and the High-Energy Electron Experiments  
87 (HEP; Mitani et al., 2018a, 2018b, 2018c) aboard the ERG satellite, which were provided from  
88 the ERG science center (Miyoshi et al., 2018b).

89 The OFA processes signals in the frequency range from a few Hz to 20 kHz detected by  
90 both triaxial magnetic search coils (Ozaki et al., 2018) and two pairs of wire probe antennas  
91 (WPT; Kasaba et al., 2017) to produce frequency spectra and spectral matrices of wave  
92 electromagnetic fields. The HFA analyzed signals from WPT in the frequency range from a few  
93 kHz to 10 MHz to produce frequency spectra of the wave electric field. The HFA spectra are  
94 examined to determine the upper hybrid resonance (UHR) frequency and thereby estimate the  
95 plasma density by referring to the electron cyclotron frequency derived from the MGF

96 measurements. The MGF measures the ambient magnetic field vector. The MEP-e provides the  
97 differential fluxes of electrons in the energy range from 7 to 87 keV. The HEP measures  
98 electrons in the energy range from 70 keV to 2 MeV. We used the wave electromagnetic field  
99 spectra, the ambient magnetic field vector, and the spin-averaged electron flux data with a time  
100 resolution of 8 s.

101 **3 Results**

102 We identified a simultaneous enhancement of both ULF waves and whistler-mode chorus  
103 emissions during the recovery phase of a magnetic storm on March 27, 2017, which was caused  
104 by the arrival of a corotating interaction region (CIR). The minimum Dst index for this storm  
105 was -74 nT. Figure 1 shows the time series of the solar wind parameters from 18:00 to 24:00  
106 Universal Time (UT) on March 27, 2017. Figures 1(a)-(e) show the solar wind speed, dynamic  
107 pressure, proton density, and the z-component of the interplanetary magnetic field (IMF) in the  
108 Geocentric Solar Magnetospheric (GSM) coordinate system, and the AL index, respectively.  
109 Figure 1(a) indicates the arrival of the high-speed coronal hole stream (cf. Miyoshi and Kataoka,  
110 2011), whose speed exceeds 600 km/s. The solar wind speed, the dynamic pressure, and the  
111 proton number density did not fluctuate significantly during this time interval (Figures 1a-c). On  
112 the other hand, Figure 1d shows Alfvénic fluctuations in the Z-component of IMF, contributing  
113 to the long-lasting intermittent enhancements of substorm activity (Figure 1e), a typical signature  
114 of CIR-driven storms (e.g., Tsurutani et al., 2006; Miyoshi et al., 2013). The AL index decreased  
115 to less than -1430 nT at 20:18 UT, indicating the development of an intense substorm.

116 We focus on the time interval from 21:30 UT to 22:00 UT, indicated by blue and red  
117 vertical lines in Figure 1. The ERG satellite was located in the range of McIlwain's L-value  
118 (McIlwain, 1961) from 6.3 to 6.1, the magnetic local time from 04:00 to 04:12, and the magnetic

latitude from -12.7 to -7.4 degrees. Figures 2(a) and (b) show the electric and magnetic field spectra, respectively, observed by OFA. The white and the red curves represent the local electron cyclotron frequency ( $f_{ce}$ ) and  $0.5 f_{ce}$ , respectively, derived from the total magnetic field intensity observed by MGF. We find periodic enhancements of lower-band chorus emissions with a period of ~2-3 minutes propagating parallel to the ambient magnetic field line (Figure S1). Figure 2(c) shows the time series of the magnetic field strength observed by the MGF, indicating the temporal variation from 145 nT to 130 nT with periodic fluctuations. Figures 2(d) and (e) show the time series of the three components of the magnetic field fluctuations observed by MGF in the Mean Field Aligned (MFA) coordinate system (cf. Takahashi et al., 1990), in which the Z component is taken toward the direction of the ambient magnetic field,  $\mathbf{B}_0$ , defined as the 200-s running averaged data of the magnetic field vector, the Y component is aligned to the direction of  $\mathbf{B}_0 \times \mathbf{r}$ , where  $\mathbf{r}$  is the position vector of the satellite taken from the center of the Earth, and the X component is taken in such a way that they form a right-handed orthogonal system, where the X- and Y-axes direct radially outward and eastward, respectively. Figure 2(d) represents the  $B_z$  component of the magnetic field fluctuations, which dominates the fluctuation of the magnetic field intensity in this time interval shown in Figure 2(c), calculated by subtracting 200-s running averages from the time series of the Z-component of the magnetic field. In Figure 2(e), we find clear sinusoidal oscillations in the  $B_y$  component and weaker oscillations in the  $B_x$  and  $B_z$  components with periods similar to each other. The fluctuations in the  $B_y$  component (green line in Figure 2e) reached over 5 nT in amplitude with a period of ~2-3 minutes. These results indicate that the observed periodic fluctuations in the magnetic field are toroidal mode Pc4-5 ULF waves. Since the time interval corresponds to the recovery phase of the strong substorm, the generation process of the observed ULF waves is thought to be related to the substorm. The

142 comparison between Figures 2(a), (b), and (e) indicates the one-to-one correspondence between  
143 the observed chorus emissions and the toroidal mode ULF waves; chorus emissions are enhanced  
144 during the westward ( $\Delta B_Y < 0$ ) phase of the toroidal mode oscillations. Figure 2(f) shows the  $X$   
145 and  $Y$  components of the electric field in the MFA coordinate system measured by EFD, where  
146 we assume  $\mathbf{E} \cdot \mathbf{B} = 0$  to obtain the electric field in the spin axis. The electric field also shows  
147 fluctuations of frequency similar to that of the magnetic field.

148 Figure 2(g) shows the omnidirectional electron number fluxes in the energy range from  
149 12.0 keV to 87.5 keV measured by MEP-e. We find flux oscillations in the energy range of 35.0-  
150 60.4 keV. In order to examine these flux oscillations quantitatively, we calculate the residual flux  
151 (c.f. Claudepierre et al., 2013) given by  $(J - J_0)/J_0$ , where  $J$  and  $J_0$  are the observed flux and its  
152 200-s running average, respectively. Figure 2(h) shows the residual fluxes in the 35.0-60.4 keV  
153 energy range. The periodic oscillations in the residual fluxes are well correlated with both  
154 waveform of the ULF waves and the intensity of the chorus emissions; the fluxes of energetic  
155 electrons enhanced at the timings of the westward phase of the toroidal mode ULF wave  
156 oscillation and the enhancements of chorus emissions. Figure 2(i) shows the pitch angle  
157 distribution of the electron flux in the energy range from 48.3 keV to 52.3 keV. We find that the  
158 periodic enhancements of the electron flux in the pitch angle range perpendicular to the  
159 background magnetic field occurred at the timings closely correlated with the ULF waves and  
160 chorus emissions. Such periodic variations of the pitch angle distribution appear not only in the  
161 50 keV but also in some neighboring energy ranges (Figure S2). The observed flux increase  
162 perpendicular to the magnetic field implies the enhancement of the temperature anisotropy of  
163 electrons.

164 **4 Discussion and Summary**

165 We showed the ERG satellite observation that the simultaneous enhancements of chorus  
166 emissions and electron flux occurred under the presence of the toroidal mode ULF waves. In  
167 order to understand the mechanism of the periodic enhancement of the observed chorus  
168 emissions, we analyzed the cyclotron resonance condition between whistler-mode waves and  
169 energetic electrons by referring to the plasma environment during the event. Previous studies  
170 suggest that chorus emissions are generated near the magnetic equator and then propagate away  
171 from the equator. Since the wave normal angle analysis by OFA shows that the observed chorus  
172 emissions propagated almost parallel to the ambient magnetic field line (Figure S1), we assume  
173 that the source region of the observed chorus emissions was located near the magnetic equator  
174 along a field line of the ERG satellite. We estimated parameters at the magnetic equator for the  
175 evaluation of the resonance condition. First, we computed the location of the equator along a  
176 field line of the satellite using the Tsyganenko-Sitnov 2005 model (Tsyganenko and Sitnov,  
177 2005) with the observed solar wind data for the field line tracing and then estimated the ambient  
178 magnetic field intensity at the equator. Second, we estimated the plasma density to be 1.46 /cc at  
179 21:40 UT and 1.96 /cc at 21:50 UT based on the UHR frequency identified in the spectra  
180 observed by HFA. Assuming that the plasma density is uniform along the magnetic field line  
181 from the location of the satellite to the magnetic equator, we used the estimated number density  
182 for the evaluation of the resonance condition. The first-order cyclotron resonance condition is  
183 considered for the resonant interaction between energetic electrons and whistler-mode waves  
184 propagating parallel to the background magnetic field. We estimated the resonant energies for a  
185 certain pitch angle of electrons for the time intervals of 21:40 UT and 21:50 UT. For the case of  
186 0 degree pitch angle, the resonant energy is estimated to be 73-168 keV at 21:40 UT and 33-89

187 keV at 21:50 UT. In the case of 45 degree pitch angle, the resonant energy is estimated to be  
188 132-293 keV at 21:40 UT and 62-161 keV at 21:50 UT. While significant periodic fluctuations  
189 do not appear in the electron flux for ~120-550 keV range observed by HEP (Figure S3),  
190 periodic fluctuations are evident in the electrons flux in the 35-60 keV range observed by MEP-  
191 e. Katoh et al. (2018) revealed by a series of electron hybrid code simulations that the condition  
192 required for the chorus generation is controlled by both the temperature anisotropy and the  
193 number density of energetic electrons. A certain level of the number density of energetic  
194 electrons is required for the chorus generation. They also showed that the required number  
195 density of energetic electrons lowers for higher temperature anisotropy. The enhancement of the  
196 electron flux in the pitch angle range perpendicular to the background magnetic field shown in  
197 Figure 2 provides favorable conditions for chorus generation. The observation results suggest  
198 that the toroidal mode ULF waves play an important role in forming the favorable condition for  
199 the enhancements of chorus emissions.

200 The intensities of chorus emissions and electron flux in the 50 keV energy range,  
201 satisfying the cyclotron resonance condition, are enhanced during the negative (westward) phase  
202 of the toroidal mode oscillations. Figure 3(a) illustrates the phase relationship between the  
203 electromagnetic field waveforms of the toroidal mode ULF waves and the flux of energetic  
204 electrons. Figures 2e-f showed that the radial component of the wave electric field ( $E_X$ ) delays by  
205 90 degrees in phase from the azimuthal component of the magnetic field ( $B_Y$ ). The phase relation  
206 between the wave electromagnetic fields observed by the ERG satellite located in the southern  
207 hemisphere suggests that the observed ULF waves are second harmonic standing waves (cf.  
208 Takahashi et al., 1996; 2011). Spectra of the waveform in the electric field indicate that the  
209 fundamental mode is also present; the wave amplitude of the fundamental mode is ~2 mV/m.

210 The oscillation of  $E_X$  results in the variation of the  $E_X \times B_0$  drift speed depending on the wave  
211 phase of the ULF wave as shown in Figure 3(a), where the labels (A) to (E) represent the wave  
212 phase every  $\pi/2$ . The observation result revealed that the residual flux of energetic electrons  
213 maximizes at the minimum of the  $B_Y$  waveform, as illustrated in Figure 3(a).

214 We consider a possible mechanism causing the distribution of energetic electrons  
215 localized at a specific phase angle of toroidal mode ULF waves. Let us assume the spatial  
216 variation of the wave phase of the toroidal mode ULF oscillation in the azimuthal direction.  
217 Considering that the wave phase increases eastward (+Y in the MFA coordinates) and that the  
218 phase relationship shown in Figure 3(a) is the spatial structure locally formed in the inner  
219 magnetosphere, a model for the observed periodic flux variations can be proposed as follows. Let  
220 us convert the time series of the waveforms shown in Figure 3(a) into a spatial structure on the  
221 equatorial plane of the magnetosphere as indicated in Figure 3(b); the wave phases  
222 corresponding to (A)-(E) in Figure 3(a) can be placed azimuthally clockwise along the electron  
223 drift path, as shown in Figure 3(b). The  $E_X$  and the  $E_X \times B_0$  drift velocity vectors at locations  
224 (A) to (E) are also shown. Figure 3(b) indicates that the modulation of the  $E_X \times B_0$  drift due to  
225 the toroidal mode ULF waves tend to converge/diverge energetic electrons azimuthally; the  
226  $E_X \times B_0$  around (D) converges electrons toward (D) and around (B) sweeps electrons away from  
227 (B). Thus, we expect the enhancement of the electron flux at the specific wave phase of the  
228 toroidal mode ULF waves corresponding to (D). In Figure 2(h), the rectangular variation of the  
229 residual flux with a single peak is found at 21:42 during the westward oscillation phase of the  $B_Y$   
230 waveform, similar to Figure 3(a). The residual flux in the time interval from 21:44 to 21:53 also  
231 maximizes during the westward oscillation phase of  $B_Y$ , but the variation is sinusoidal rather than  
232 rectangular. The sinusoidal variation may indicate a transition stage of the convergence of the

233 electron flux due to the ULF waves. A rectangular flux variation with a single peak can be  
 234 expected in an ideal case that electrons around (B) in Figure 3(a) are completely swept out and  
 235 fully converged around (D). A sinusoidal flux variation can be expected during a transition stage  
 236 forming a flux peak around (D) with a depletion around (B), corresponding to the eastward  
 237 oscillation phase of  $B_Y$ . Since a single peak of the flux variation indicated in Figure 3 requires an  
 238 ideal situation, sinusoidal variation would be typical in the magnetosphere.

239 Considering that the spatial structure formed by the regions of the enhanced electron flux  
 240 moves with the wave phase variation of the ULF waves, we expect that the whole spatial  
 241 structure drifts eastward with the phase velocity of the ULF wave. Then we can reconstruct the  
 242 time series of the waveforms (Figure 3a) from the spatial distribution (Figure 3b); the flux  
 243 enhancement is observed by the satellite at the timings corresponding to the wave phase angle  
 244 corresponding to (D) in Figure 3(a). This model suggests that the dense region caused by the  
 245 azimuthal inhomogeneity of the  $\mathbf{E}_X \times \mathbf{B}_0$  drift corresponds to the flux enhancement observed by  
 246 the ERG satellite.

247 The flux enhancement of the proposed model becomes significant in a case where the  
 248  $\mathbf{E}_X \times \mathbf{B}_0$  drift speed is comparable to the magnetic drift speed of energetic electrons. We  
 249 estimate the  $\mathbf{E}_X \times \mathbf{B}_0$  drift speed from the electric and magnetic field data observed by EFD and  
 250 MGF. According to the ULF amplitude in the electric field of 2 mV/m and the background  
 251 magnetic field intensity of 130 nT, the  $\mathbf{E}_X \times \mathbf{B}_0$  drift speed is estimated to be about 15.4 km/s.  
 252 On the other hand, the bounce averaged drift period  $\langle \tau_d \rangle$  [sec] of energetic electrons in the dipole  
 253 field is given by (cf. Walt, 1994)

$$254 \quad \langle \tau_d \rangle = \frac{\pi e B_E R_E^2}{LW} \left[ 1 - \frac{1}{3} (\sin \alpha_{eq})^{0.62} \right], \quad (1)$$

255 where  $e$  is the elementary charge,  $B_E$  is the equatorial magnetic field intensity on the surface of  
 256 the Earth, about 31,100 nT,  $R_E$  is the Earth's radius,  $L$  is L-value,  $W$  and  $\alpha_{eq}$  are the kinetic  
 257 energy and the equatorial pitch angle of electrons, respectively. The drift speed  $V_B$  of electrons of  
 258 the 90 degree pitch angle is given by

$$259 \quad V_B = \frac{2\pi LR_E}{\langle \tau_d \rangle} = \frac{2W}{eB_E R_E} \frac{L^2}{.} \quad (2)$$

260 Then  $V_B$  of electrons in the energy range of 35-60 keV at L=6 is estimated to be 12.3-20.7 km/s,  
 261 comparable to the estimated  $E_X \times B_0$  drift speed. Since the bounce period is much shorter than  
 262 both the time scale of the drift motion of energetic electrons and the wave period of the observed  
 263 ULF waves, we can neglect the azimuthal motion of energetic electrons during one bounce  
 264 period. The bounce period  $\tau_b$  [sec] of energetic electrons in the dipole field is given by (cf. Walt,  
 265 1994)

$$266 \quad \tau_b = 0.117 L \frac{c}{v} \left[ 1 - 0.4635 (\sin \alpha_{eq})^{3/4} \right], \quad (3)$$

267 where  $v$  denotes the speed of electron and  $c$  represents the speed of light. For electrons of the 60  
 268 degree pitch angle in the energy range of 35-60 keV,  $\tau_b$  is estimated to be 0.16-0.2 seconds.

269 In the higher latitude region away from the equator, where bouncing electrons spend most  
 270 of the bouncing period, the effects of the azimuthal inhomogeneity of the  $E_X \times B_0$  drift speed on  
 271 energetic electrons are thought to be weaker because the ambient magnetic field intensity is  
 272 stronger and the  $E_X \times B_0$  drift speed is slower. The electric field of the fundamental mode at the  
 273 equator should be larger than those observed. Thus, the amplitude of the flux variation of  
 274 bouncing electrons is thought to be smaller than that of near-equatorially mirroring electrons.  
 275 Although quantitative evaluation should be performed in our future study, this difference in the

276 flux variation according to the equatorial pitch angle may cause the observed pitch angle  
277 dependence of energetic electrons shown in Figure 2(i).

278 Finally, we discuss the spatial scale of the interaction region associated with the ULF  
279 waves, chorus emissions, and energetic electrons. The proposed model suggests that the  
280 azimuthally localized electron structure is drifting eastward with the phase velocity of ULF  
281 waves. The longitudinal wavelength is estimated to be 2,310 km using the wave period 150 sec  
282 and the drift speed of 15.4 km/s, corresponding to the m number of ~17. Although the estimated  
283 spatial scale is smaller than those of the externally excited toroidal mode ULF waves typically  
284 observed in the inner magnetosphere [cf. Takahashi, 2016] and is rather comparable to those of  
285 internally driven poloidal mode ULF waves, previous studies reported eastward-propagating  
286 internally driven ULF waves with a similar azimuthal wavenumber during a substorm [James et  
287 al., 2013; Hori et al., 2018]. Validation of the proposed scenario on the modulation of energetic  
288 electrons by toroidal mode ULF waves should be conducted by a statistical survey of the data  
289 and by numerical simulations, which are left for future studies.

290

## 291 **Data Availability Statement**

292 The present study analyzed PWE/OFA L2-v02\_02 data (doi:10.34515/DATA.ERG-08000),  
293 PWE/EFD L2-v05\_01 data (doi:10.34515/DATA.ERG-07000), PWE/HFA L2-v01\_02 data  
294 (doi:10.34515/DATA.ERG-10000), MGF-L2 8 sec spin-averaged data v03\_04  
295 (doi:10.34515/DATA.ERG-06001), MEP-e-L2 3-D flux data v01\_01  
296 (doi:10.34515/DATA.ERG-02000), MEP-e-L2 omniflux data v01\_02  
297 (doi:10.34515/DATA.ERG-02001), HEP-L2 omniflux data v03\_01 (doi:10.34515/DATA.ERG-  
298 01001), HEP-L3 pitch angle sorted electron flux data v01\_01 (doi:10.34515/DATA.ERG-

299 01002), and Orbit L2 v03 data (doi:10.34515/DATA.ERG-12000). The SPEDAS software  
300 (Angelopoulos et al., 2019) and ERG Plug-in tools were used for data analysis.

301

302 **Acknowledgments**

303 This study is supported by Grants-in-Aid for Scientific Research (15H05747, 18H03727,  
304 20H01959, and 20K04052) of Japan Society for the Promotion of Science. This research is also  
305 supported by the joint research program of the Institute for Space-Earth Environmental Research,  
306 Nagoya University.

307

308 **References**

- 309 Angelopoulos, V., Cruce, P., Drozdov, A., Grimes, E. W., Hatzigeorgiu, N., King, D. A., et al.  
310 (2019) The Space Physics Environment Data Analysis System (SPEDAS), *Space Sci.*  
311 *Rev.*, 215, 9, doi:10.1007/s11214-018-0576-4.
- 312 Baumjohann, W., and R. A. Treumann (1996), "Basic Space Plasma Physics", London, Imperial  
313 College Press.
- 314 Claudepierre, S. G., I. R. Mann, K. Takahashi, J. F. Fennell, M. K. Hudson, J. B. Blake, J. L.  
315 Roeder, J. H. Clemons, H. E. Spence, G. D. Reeves, D. N. Baker, H. O. Funsten, R. H.  
316 W. Friedel, M. G. Henderson, C. A. Kletzing, W. S. Kurth, R. J. MacDowall, C. W.  
317 Smith, and J. R. Wygant (2013), Van Allen Probes observation of localized drift  
318 resonance between poloidal mode ultra-low frequency waves and 60 keV electrons,  
319 *Geophys. Res. Lett.*, 40, 4491–4497, doi: 10.1002/grl.50901.
- 320 Coroniti, F. V., and C. F. Kennel (1970), Electron Precipitation Pulsations, *J. Geophys. Res.*, 75,  
321 1279-1289.
- 322 Elkington, S. R., M. K. Hudson, and A. A. Chan (1999), Acceleration of relativistic electrons via  
323 drift-resonant interaction with toroidal-mode Pc-5 ULF oscillations, *Geophys. Res. Lett.*,  
324 26, 3273-3.
- 325 Hori, T., N. Nishitani, S. G. Shepherd, J. M. Ruohoniemi, M. Connors, M. Teramoto, S. Nakano,  
326 K. Seki, N. Takahashi, S. Kasahara, S. Yokota, T. Mitani, T. Takashima, N. Higashio, A.  
327 Matsuoka, K. Asamura, Y. Kazama, S.-Y. Wang, S. W. Y. Tam, T.-F. Chang, B.-J.  
328 Wang, Y. Miyoshi, I. Shinohara (2018), Substorm-Associated Ionospheric Flow  
329 Fluctuations During the 27 March 2017 Magnetic Storm: SuperDARN-Arase  
330 Conjunction, *Geophys. Res. Lett.*, 45, 18, 9441-9449, doi:10.1029/2018GL079777.

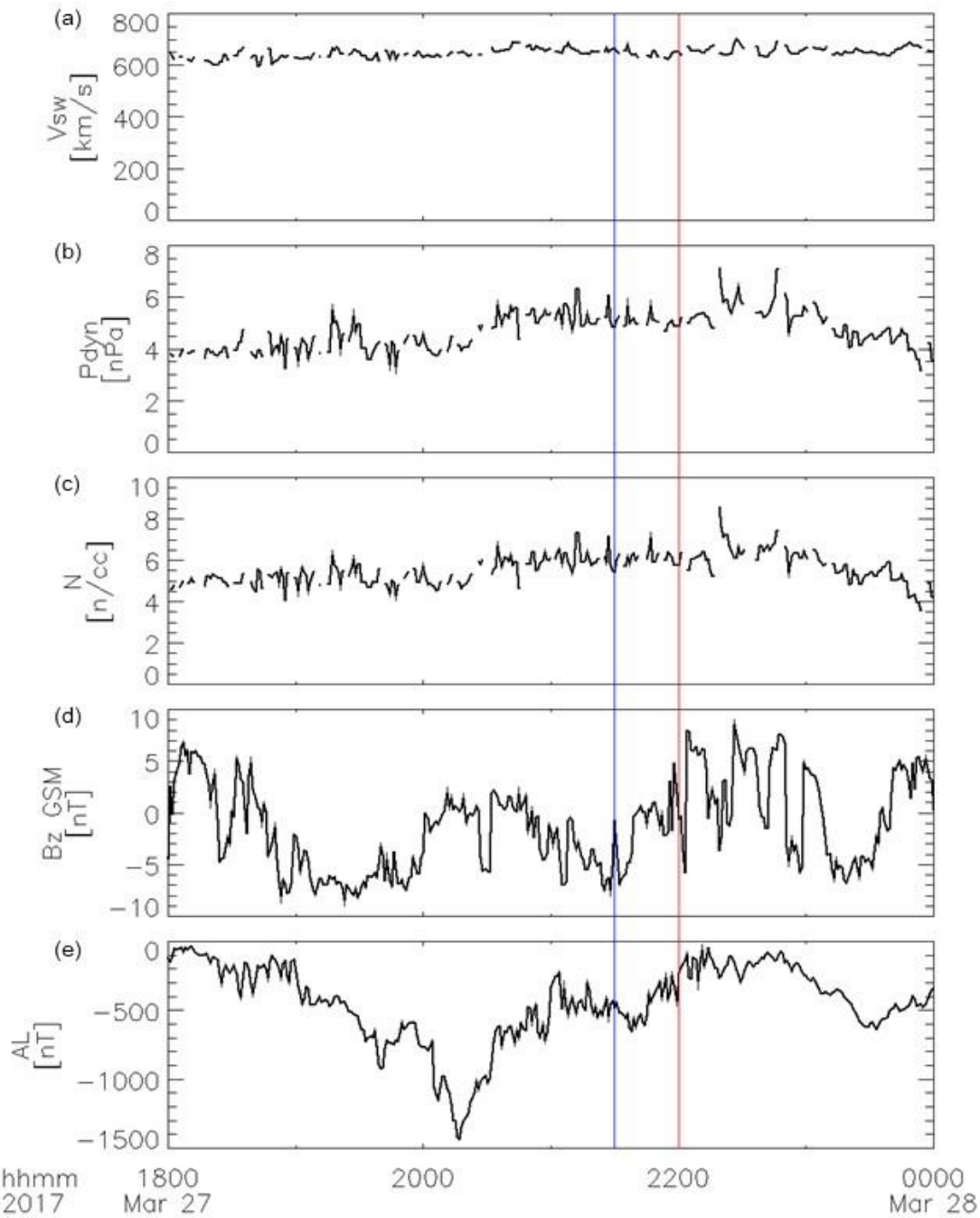
- 331 Hori, T., T. Mitani, A. Matsuoka, M. Teramoto, I. Park, T. Takashima, Y. Miyoshi, and I.  
 332 Shinohara (2020), The HEP instrument Level-3 pitch angle sorted electron flux data of  
 333 Exploration of energization and Radiation in Geospace (ERG) Arase satellite,  
 334 DOI:10.34515/DATA.ERG-01002.
- 335 James, M. K., T. K. Yeoman, P. N. Mager, D. Yu. Klimushkin (2013), The spatio-temporal  
 336 characteristics of ULF waves driven by substorm injected particles, *J. Geophys. Res.*  
 337 *Space Phys.*, 118, 4, 1737-1749, doi:10.1002/jgra.50131.
- 338 Jaynes, A. N., M. R. Lessard, K. Takahashi, A. F. Ali, D. M. Malaspina, R. G. Michell, E. L.  
 339 Spanswick, D. N. Baker, J. B. Blake, C. Cully, E. F. Donovan, C. A. Kletzing, G. D.  
 340 Reeves, M. Samara, H. E. Spence, and J. R. Wygant (2015), Correlated Pc4–5 ULF  
 341 waves, whistler-mode chorus and pulsating aurora observed by the Van Allen Probes and  
 342 ground-based systems, *J. Geophys. Res.*, 120, 8749–8761, doi:10.1002/2015JA021380.
- 343 Kasaba, Y., K. Ishisaka, Y. Kasahara, T. Imachi, S. Yagitani, H. Kojima, S. Matsuda, M. Shoji,  
 344 S. Kurita, T. Hori, A. Shinburi, M. Teramoto, Y. Miyoshi, T. Nakagawa, N. Takahashi,  
 345 Y. Nishimura, A. Matsuoka, A. Kumamoto, F. Tsuchiya, and R. Nomura (2017), Wire  
 346 Probe Antenna (WPT) and Electric Field Detector (EFD) of Plasma Wave Experiment  
 347 (PWE) aboard the Arase satellite: specifications and initial evaluation results, *Earth*  
 348 *Planets Space*, 69, 174, doi:10.1186/s40623-017-0760-x.
- 349 Kasahara, S., Y. Miyoshi, S. Yokota, T. Mitani, Y. Kasahara, S. Matsuda, A. Kumamoto, A.  
 350 Matsuoka, Y. Kazama, H. U. Frey, V. Angelopoulos, S. Kurita, K. Keika, K. Seki, and I.  
 351 Shinohara (2018a), Pulsating aurora from electron scattering by chorus waves, *Nature*,  
 352 554, 337-340, doi:10.1038/nature25505.
- 353 Kasahara, S., S. Yokota, T. Mitani, K. Asamura, M. Hirahara, Y. Shibano, and T. Takashima  
 354 (2018b), Medium-Energy Particle experiments - electron analyser (MEP-e) for the  
 355 Exploration of energization and Radiation in Geospace (ERG) mission, *Earth Planets*  
 356 *Space*, 70, 69, doi:10.1186/s40623-018-0847-z.
- 357 Kasahara, S., S. Yokota, T. Hori, K. Keika, Y. Miyoshi, and I. Shinohara (2018c), The MEP-e  
 358 instrument Level-2 3-D flux data of Exploration of energization and Radiation in  
 359 Geospace (ERG) Arase satellite, DOI:10.34515/DATA.ERG-02000.
- 360 Kasahara, Y., Y. Kasaba, H. Kojima, S. Yagitani, K. Ishisaka, A. Kumamoto, F. Tsuchiya, M.  
 361 Ozaki, S. Matsuda, T. Imachi, Y. Miyoshi, M. Hikishima, Y. Katoh, M. Ota, M. Shoji, A.  
 362 Matsuoka, and I. Shinohara (2018a), The Plasma Wave Experiment (PWE) on board the  
 363 Arase (ERG) satellite, *Earth Planets Space*, 70, 86, doi:10.1186/s40623-018-0842-4.
- 364 Kasahara, Y., Y. Kasaba, S. Matsuda, M. Shoji, T. Nakagawa, K. Ishisaka, S. Nakamura, M.  
 365 Kitahara, Y. Miyoshi, and I. Shinohara (2018b), The PWE/EFD instrument Level-2 spin-  
 366 fit electric field data of Exploration of energization and Radiation in Geospace (ERG)  
 367 Arase satellite, DOI:10.34515/DATA.ERG-07000.
- 368 Kasahara, Y., H. Kojima, S. Matsuda, M. Ozaki, S. Yagitani, M. Shoji, S. Nakamura, M.  
 369 Kitahara, Y. Miyoshi, and I. Shinohara (2018c), The PWE/OFA instrument Level-2  
 370 spectrum data of Exploration of energization and Radiation in Geospace (ERG) Arase  
 371 satellite, DOI:10.34515/DATA.ERG-08000.

- 372 Kasahara, Y., A. Kumamoto, F. Tsuchiya, S. Matsuda, M. Shoji, S. Nakamura, M. Kitahara, I.  
373 Shinohara, and Y. Miyoshi (2018d), The PWE/HFA instrument Level-2 spectrum data of  
374 Exploration of energization and Radiation in Geospace (ERG) Arase satellite,  
375 DOI:10.34515/DATA.ERG-10000.
- 376 Katoh, Y., Omura, Y., Miyake, Y., Usui, H., and Nakashima, H. (2018) Dependence of  
377 generation of whistler mode chorus emissions on the temperature anisotropy and density  
378 of energetic electrons in the Earth's inner magnetosphere, *J. Geophys. Res.: Space Phys.*,  
379 123, 1165–1177, doi.org/10.1002/2017JA024801.
- 380 Kumamoto, A., F. Tsuchiya, Y. Kasahara, Y. Kasaba, H. Kojima, S. Yagitani, K. Ishisaka, T.  
381 Imachi, M. Ozaki, S. Matsuda, M. Shoji, A. Matsuoka, Y. Katoh, Y. Miyoshi, and T.  
382 Obara (2018), High Frequency Analyzer (HFA) of Plasma Wave Experiment (PWE)  
383 onboard the Arase spacecraft, *Earth Planets Space*, 70, 82, doi:10.1186/s40623-018-  
384 0854-0.
- 385 Li, W., R. M. Thorne, J. Bortnik, Y. Nishimura, and V. Angelopoulos (2011), Modulation of  
386 whistler mode chorus waves: 1. Role of compressional Pc4–5 pulsations, *J. Geophys.  
387 Res.*, 116, A06205, doi:10.1029/2010JA016312.
- 388 Liu, N., Z. Su, Z. Gao, H. Zheng, Y. Wang, and S. Wang (2019), Magnetospheric chorus,  
389 exohiss, and magnetosonic emissions simultaneously modulated by fundamental toroidal  
390 standing Alfvén waves following solar wind dynamic pressure fluctuations, *Geophys.  
391 Res. Lett.*, 46, 1900–1910, doi:10.1029/2018GL081500.
- 392 Matsuda, S., Y. Kasahara, H. Kojima, Y. Kasaba, S. Yagitani, M. Ozaki, T. Imachi, K. Ishisaka,  
393 A. Kumamoto, F. Tsuchiya, M. Ota, S. Kurita, Y. Miyoshi, M. Hikishima, A. Matsuoka  
394 and I. Shinohara (2018), Onboard Software of Plasma Wave Experiment aboard Arase:  
395 Instrument Management and Signal Processing of Waveform Capture/Onboard  
396 Frequency Analyzer, *Earth Planets Space*, 70, 75, doi:10.1186/s40623-018-0838-0.
- 397 Matsuoka, A., M. Teramoto, R. Nomura, M. Nosé, A. Fujimoto, Y. Tanaka, M. Shinohara, T.  
398 Nagatsuma, K. Shiokawa, Y. Obana, Y. Miyoshi, M. Mita, T. Takashima, and I.  
399 Shinohara (2018a), The ARASE(ERG) magnetic field investigation, *Earth Planets Space*,  
400 70, 43, doi:10.1186/s40623-018-0800-1.
- 401 Matsuoka, A., M. Teramoto, S. Imajo, S. Kurita, Y. Miyoshi, and I. Shinohara (2018b), The  
402 MGF instrument Level-2 spinfit magnetic field data of Exploration of energization and  
403 Radiation in Geospace (ERG) Arase satellite, DOI:10.34515/DATA.ERG-06001.
- 404 McIlwain, C. E. (1961), Coordinates for mapping the distribution of magnetically trapped  
405 particles, *J. Geophys. Res.*, 66, 3681–3691, doi:10.1029/JZ066i011p03681.
- 406 Mitani, T., T. Takashima, S. Kasahara, W. Miyake and M. Hirahara (2018a), High-energy  
407 electron experiments (HEP) aboard the ERG (Arase) satellite, *Earth, Planets and  
408 Space*, 70, 77, doi:10.1186/s40623-018-0853-1.
- 409 Mitani, T., T. Hori, I. Park, T. Takashima, Y. Miyoshi, and I. Shinohara (2018b), The HEP  
410 instrument Level-2 omni-directional flux data of Exploration of energization and  
411 Radiation in Geospace (ERG) Arase satellite, DOI:10.34515/DATA.ERG-01001, 2018.

- 412 Miyoshi, Y., and R. Kataoka (2011), Solar cycle variations of outer radiation belt and its  
413 relationship to solar wind structure dependences, *J. Atmos. Sol-Terr. Phys.*, 73, 1, 77-87,  
414 doi:10.1016/j.jastp.2010.09.031.
- 415 Miyoshi, Y., Y. Katoh, T. Nishiyama, T. Sakanoi, K. Asamura, and M. Hirahara, Time of flight  
416 analysis of pulsating aurora electrons, considering wave-particle interactions with  
417 propagating whistler mode waves, *J. Geophys. Res.*, 115, A10312,  
418 doi:10.1029/2009JA015127, 2010.
- 419 Miyoshi, Y., R. Kataoka, Y. Kasahara, A. Kumamoto, T. Nagai, and M. Thomsen, High-speed  
420 solar wind with southward interplanetary magnetic field causes relativistic electron flux  
421 enhancement of the outer radiation belt via enhanced condition of whistler waves,  
422 *Geophys. Res. Lett.*, 40, doi:10.1002/grl.50916, 2013.
- 423 Miyoshi, Y. S. Saito, K. Seki, T. Nishiyama, R. Kataoka, K. Asamura, Y. Katoh, Y. Ebihara, T.  
424 Sakanoi, M. Hirahara, S. Oyama, S. Kurita, and O. Santolik, Relation between energy  
425 spectra of pulsating aurora electrons and frequency spectra of whistler-mode chorus  
426 waves, *J. Geophys. Res.*, 120, 7728-7736, doi:10.1002/2015JA021562, 2015.
- 427 Miyoshi, Y., I. Shinohara,, T. Takashima, K. Asamura, N. Higashio, T. Mitani, S. Kasahara, S.  
428 Yokota, Y. Kazama, S.-Y. Wang, S. W. Tam, P. T. P Ho, Y. Kasahara, Y. Kasaba, S.  
429 Yagitani, A. Matsuoka, H. Kojima, H. Katoh, K. Shiokawa, and K. Seki (2018a),  
430 Geospace Exploration Project ERG, *Earth Planets Space*, 70, 101, doi:10.1186/s40623-  
431 018-0862-0.
- 432 Miyoshi, Y., T. Hori, M. Shoji, M. Teramoto, T. F. Chang, S. Matsuda, S. Kurita, T. Segawa, N.  
433 Umemura, K. Keika, Y. Miyashita, Y. Tanaka, N. Nishitani, T. Takashima, and I.  
434 Shinohara (2018b), The ERG Science Center, *Earth Planets Space*, 70, 96,  
435 doi:10.1186/s40623-018-0867-8.
- 436 Miyoshi, Y., I. Shinohara and C.-W. Jun (2018c), The Level-2 orbit data of Exploration of  
437 energization and Radiation in Geospace (ERG) Arase satellite, 10.34515/DATA.ERG-  
438 12000.
- 439 Miyoshi, Y., K. Hosokawa, S. Kurita, S.-I. Oyama, Y. Ogawa, S. Saito, I. Shinohara, A. Kero, E.  
440 Turunen, P. T. Verronen, S. Kasahara, S. Yokota, T. Mitani, T. Takashima, N. Higashio,  
441 Y. Kasahara, S. Masuda, F. Tsuchiya, A. Kumamoto, A. Matsuoka, T. Hori, K. Keika, M.  
442 Shoji, M. Teramoto, S. Imajo, C. Jun, and S. Nakamura (2021), Penetration of MeV  
443 electrons into the mesosphere accompanying pulsating aurorae, *Scientific Reports*, 11,  
444 13724, doi:10.1038/s41598-021-92611-3.
- 445 Nishimura, Y., J. Bortnik, W. Li, R. M. Thorne, L. R. Lyons, V. Angelopoulos, S. B. Mende, J.  
446 W. Bonnell, O. Le Contel, C. Cully, R. Ergun, U. Auster (2010), Identifying the Driver of  
447 Pulsating Aurora, *Science*, 330, 81-84, doi:10.1126/science.1193186.
- 448 Omura, Y. (2021), Nonlinear wave growth theory of whistler-mode chorus and hiss emissions in  
449 the magnetosphere, *Earth Planets Space*, 73, 95, doi:10.1186/s40623-021-01380-w.
- 450 Omura, Y., Y. Katoh, and D. Summers (2008), Theory and simulation of the generation of  
451 whistler-mode chorus, *J. Geophys. Res.*, 113, A04223, doi:10.1029/2007JA012622.

- 452 Omura, Y., M. Hikishima, Y. Katoh, D. Summers, and S. Yagitani (2009), Nonlinear  
453 mechanisms of lower-band and upper-band VLF chorus emissions in the magnetosphere,  
454 *J. Geophys. Res.*, 114, A07217, doi:10.1029/2009JA014206.
- 455 Ozaki, M., S. Yagitani, Y. Kasahara, H. Kojima, Y. Kasaba, A. Kumamoto, F. Tsuchiya, S.  
456 Matsuda, A. Matsuoka, T. Sasaki, and T. Yumoto (2018), Magnetic Search Coil (MSC)  
457 of Plasma Wave Experiment (PWE) aboard the Arase (ERG) satellite, *Earth Planets  
458 Space*, 70, 76, doi:10.1186/s40623-018-0837-1.
- 459 Southwood, D. J., J. W. Dungey, and R. J. Etherington (1969), Bounce resonant interaction  
460 between pulsations and trapped particles, *Planet. Space Sci.*, 17, 349-361.
- 461 Southwood, D. J., and M. G. Kivelson (1981), Charged Particle Behavior in Low-Frequency  
462 Geomagnetic Pulsations 1. Transverse Waves, *J. Geophys. Res.*, 86, 5643-5655.
- 463 Takahashi, K. (2016), ULF waves in the inner magnetosphere. In A. Keiling, D.-H. Lee, & V.  
464 Nakariakov (Eds.), *Low-frequency waves in space plasmas* (pp. 51–63).  
465 <https://doi.org/10.1002/9781119055006.ch4>
- 466 Takahashi, K., C. Z. Cheng, R. W. McEntire, and L. M. Kistler (1990), Observation and theory  
467 of Pc 5 waves with harmonically related transverse and compressional components, *J.  
468 Geophys. Res.*, 95(A2), 977-989.
- 469 Takahashi, K., B. J. Anderson, and S. Ohtani (1996), Multisatellite study of nightside transient  
470 toroidal waves, *J. Geophys. Res.*, 101, 24,815-24,825, doi:10.1029/96JA02045.
- 471 Takahashi, K., K.-H. Glassmeier, V. Angelopoulos, J. Bonnell, Y. Nishimura, H. J. Singer, and  
472 C. T. Russell (2011), Multisatellite observations of a giant pulsation event, *J. Geophys.  
473 Res.*, 116, A11223, doi:10.1029/2011JA016955.
- 474 Tsurutani, B. T., W. D. Gonzalez, A. L. C. Gonzalez, F. L. Guarnieri, N. Gopalswamy, M.  
475 Grande, Y. Kamide, Y. Kasahara, G. Lu, I. Mann, R. McPherron, F. Soraas, V.  
476 Vasylunas (2006), Corotating solar wind streams and recurrent geomagnetic activity: A  
477 review, *J. Geophys. Res.*, 111, A07S01, doi:10.1029/2005JA011273.
- 478 Tsytganenko, N. A., and M. I. Sitnov (2005), Modeling the dynamics of the inner magnetosphere  
479 during strong geomagnetic storms, *J. Geophys. Res.*, 110, A03208, doi:  
480 10.1029/2004JA010798.
- 481 Walt, M. (1994). *Introduction to Geomagnetically Trapped Radiation* (Cambridge Atmospheric  
482 and Space Science Series). Cambridge: Cambridge University Press.  
483 doi:10.1017/CBO9780511524981.
- 484 Xia, Z., L. Chen, L. Dai, S. G. Claudepierre, A. A. Chan, A. R. Soto-Chavez, and G. D. Reeves  
485 (2016), Modulation of chorus intensity by ULF waves deep in the inner magnetosphere,  
486 *Geophys. Res. Lett.*, 43, 9444–9452, doi:10.1002/2016GL070280.
- 487 Zhang, X.-J., L. Chen, A. V. Artemyev, V. Angelopoulos, and X. Liu (2019) Periodic excitation  
488 of chorus and ECH waves modulated by ultralow frequency compressions, *J. Geophys.  
489 Res.*, 124, 8535-8550, doi:10.1029/2019JA027201.

490



491

492

**Figure 1.** The time series of (a) the solar wind speed, (b) the dynamic pressure, (c) the density, (d) the  $B_z$  component of Interplanetary Magnetic Field (IMF) in the Geocentric Solar Magnetospheric (GSM) coordinate system, and (e) AL index from 18:00 UT to 24:00UT on March 27, 2017. Blue and red vertical lines indicate the start and end time of the time interval shown in Figure 2, respectively.

493

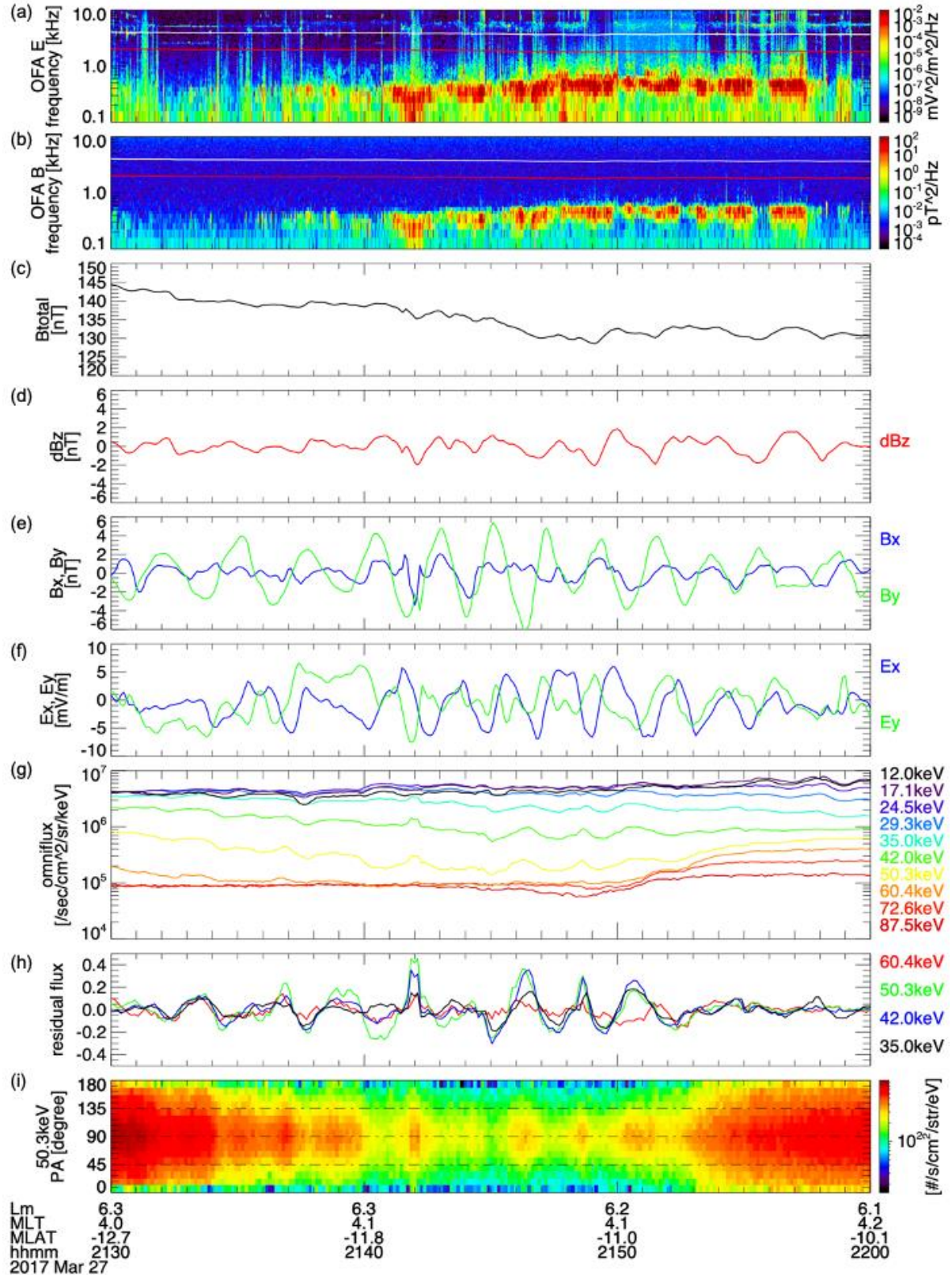
494

495

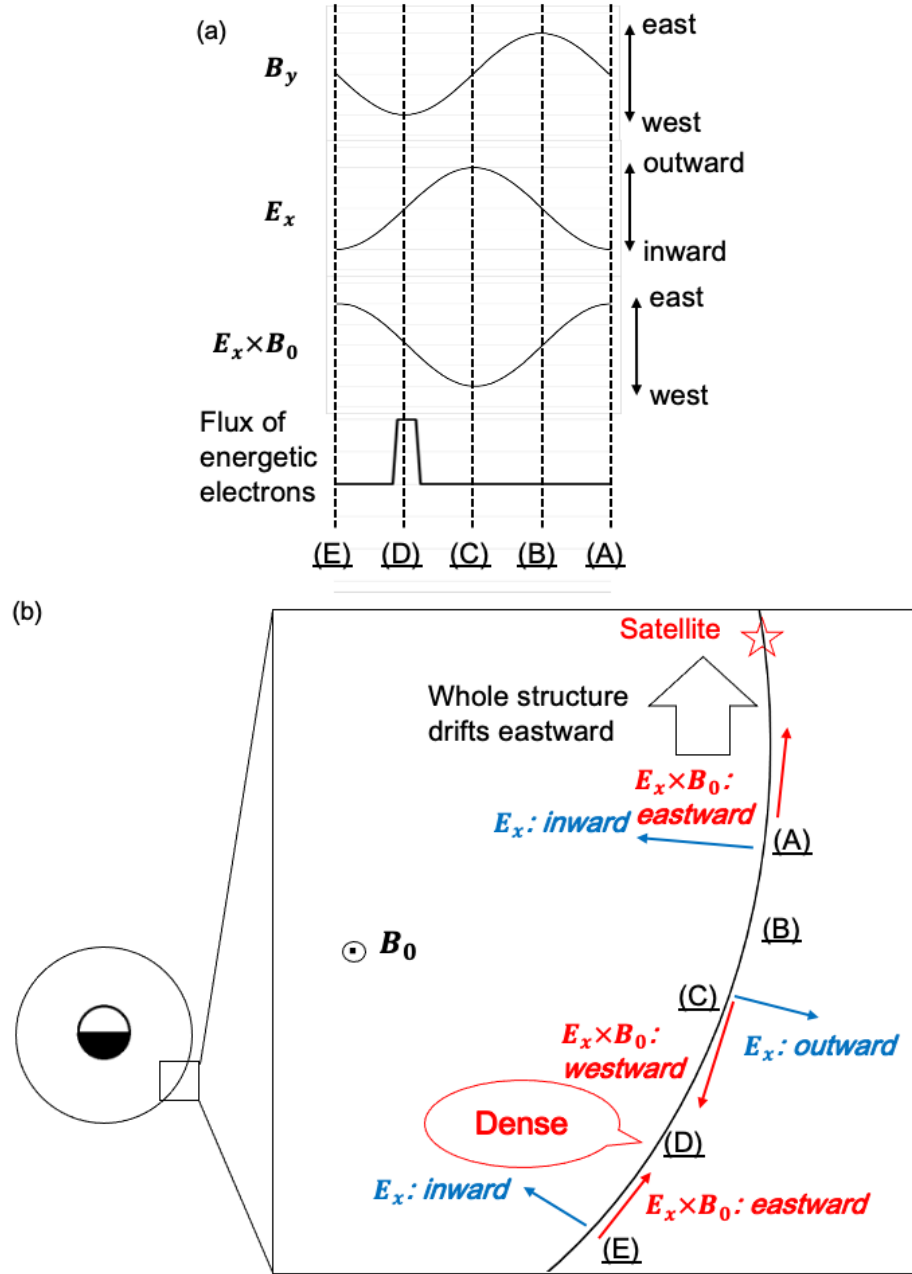
496

497

498



500 **Figure 2.** Observation results of the ERG satellite from 21:30 UT to 22:00 UT on March 27,  
501 2017. (a) Wave electric field and (b) magnetic field spectra observed by the OFA of the PWE  
502 along with the  $f_{ce}$  (shown in white) and the  $0.5f_{ce}$  (red) calculated from the magnetic field data  
503 from the MGF. (c) The total magnetic field intensity. (d) The  $B_z$ , (e)  $B_x$  (blue), and  $B_y$  (green)  
504 components of the magnetic field in the MFA coordinate system. (f) The  $E_x$  (blue) and  $E_y$   
505 (green) components of the electric field in the MFA coordinate system. (g) The omnidirectional  
506 electron fluxes from 12.0 to 87.5 keV energy range. (h) the residual fluxes calculated from the  
507 omnidirectional electron number fluxes in the 35.0 keV (black), 42.0 keV (blue), 50.3 keV  
508 (green), and 60.4 keV (red) energy range. (i) The pitch angle distribution in the 50.3 keV energy  
509 range observed by the MEP-e.  
510



511  
512  
513  
514  
515  
516  
517

**Figure 3.** Schematic illustration of (a) the phase relationship among the wave electromagnetic field of toroidal mode standing ULF waves, the  $E_x \times B_0$  drift caused by the wave electric field and the ambient magnetic field, and the fluctuation components of energetic electrons observed and expected to be observed by the satellite and (b) expected spatial structure along the drift path of energetic electrons looked down from north of the Earth.